NANO · MICRO small
www.small-journal.com

Quantification of the Activator and Sensitizer Ion Distributions in $NaYF_4$:Yb^{3+}, Er^{3+} Upconverting Nanoparticles Via Depth-Profiling with Tender X-Ray Photoemission

Pip C. J. Clark, Elina Andresen, Michael J. Sear, Marco Favaro, Leonardo Girardi, Roel van de Krol, Ute Resch-Genger, and David E. Starr**

The spatial distribution and concentration of lanthanide activator and sensitizer dopant ions are of key importance for the luminescence color and efficiency of upconverting nanoparticles (UCNPs). Quantifying dopant ion distributions and intermixing, and correlating them with synthesis methods require suitable analytical techniques. Here, X-ray photoelectron spectroscopy depth-profiling with tender X-rays (2000–6000 eV), providing probe depths ideally matched to UCNP sizes, is used to measure the depth-dependent concentration ratios of Er^{3+} to Yb^{3+}, $[Er^{3+}]/[Yb^{3+}]$, in three types of UCNPs prepared using different reagents and synthesis methods. This is combined with data simulations and inductively coupled plasma-optical emission spectroscopy (ICP-OES) measurements of the lanthanide ion concentrations to construct models of the UCNPs' dopant ion distributions. The UCNP sizes and architectures are chosen to demonstrate the potential of this approach. Core-only UCNPs synthesized with $XCl_3{\cdot}6H_2O$ precursors (β-phase) exhibit a homogeneous distribution of lanthanide ions, but a slightly surface-enhanced $[Er^{3+}]/[Yb^{3+}]$ is observed for UCNPs prepared with trifluroacetate precursors (α-phase). Examination of Yb-core@Er-shell UCNPs reveals a co-doped, intermixed region between the single-doped core and shell. The impact of these different dopant ion distributions on the UCNP's optical properties is discussed to highlight their importance for UCNP functionality and the design of efficient UCNPs.

1. Introduction

Spectrally shifting, upconverting nanoparticles (UCNPs), based on $NaYF_4$ that show photoluminescence (PL) in the ultraviolet (UV), visible, and near-infrared (NIR) regions, have drawn considerable attention due to their potential for applications in photocatalysis,[1] bioimaging and sensing,[2–6] non-invasive luminescence thermometry,[7,8] drug delivery,[9–11] extending the absorption range of solar energy devices,[12–15] and use in other optical devices.[16–18] During upconversion with Yb^{3+} and Er^{3+} doped $NaYF_4$ UCNPs, the sensitizer ions (Yb^{3+}) absorb NIR photons and transfer the energy of two or more photons to an activator ion (Er^{3+}). Subsequently, the excited Er^{3+} ions emit a multitude of narrow emission bands of shorter wavelength including the most prominent green (510–570 nm; maxima λ_{em} at 525 and 545 nm) and red (630–685 nm; maximum λ_{em} = 655 nm) emission bands.[19–21]

Increasing upconversion efficiency and enhancing the brightness of UCNPs are

P. C. J. Clark, M. J. Sear, M. Favaro, R. van de Krol, D. E. Starr
Institute for Solar Fuels
Helmholtz-Zentrum Berlin für Materialien und Energie GmbH
Hahn-Meitner-Platz 1, 14109 Berlin, Germany
E-mail: david.starr@helmholtz-berlin.de

The ORCID identification number(s) for the author(s) of this article can be found under https://doi.org/10.1002/smll.202107976.

DOI: 10.1002/smll.202107976

E. Andresen, U. Resch-Genger
BAM Federal Institute for Materials Research and Testing
Division 1.10 Biophotonics, Richard-Willstätter-Str. 11, 12489 Berlin, Germany
E-mail: ute.resch@bam.de

L. Girardi
Department of Chemical Sciences and INSTM Unit
University of Padova
Via F. Marzolo 1, Padova 35131, Italy

among the main challenges hindering their technological adoption. There are various types of quenching processes that lead to a reduced upconversion efficiency.[22] First, a common problem in all luminescent nanoparticles, is surface quenching. Surface quenching can be caused by defect sites on the nanoparticle surface and/or the high energy vibrations of −OH, −NH, or $-CH_2$ groups at or close to the particle surface.[23–25] These groups can also lead to quenching of the upconversion luminescence (UCL) when present within the UCNPs.[22] A common strategy to reduce surface quenching is to shield the light-absorbing and emitting lanthanide dopants with an inert shell of dopant-free material, for example, $NaYF_4$.[25–30] The ability to confine the sensitizer and activator ions in the core of such core@shell structures is partially affected by core/shell intermixing during the shell formation procedures.[31,32] Another type of UCL quenching is concentration quenching[33–35] caused by cross-relaxation (CR) between dopant ions, particularly the activator ions, at higher concentrations. Concentration quenching can be mitigated by spatially separating the sensitizer and activator ions through various core@shell, multi-shell, and sandwich structures,[26,36–41] or clustering of sensitizer ions (Yb^{3+}).[19] Concentration quenching can also be alleviated by innovative excitation schemes, or high excitation power densities such that all or nearly all of the sensitizer ions are excited, as shown by recent microscopic studies.[42,43] In addition to a loss in UCL intensity, both quenching pathways also affect the spectral characteristics, that is, color, of UCL.[44] These reports underline the key roles that the spatial distribution and concentration of activator and sensitizer ions play in surface and concentration quenching, and call for suitable analytical methods to measure them.[32,45]

A powerful tool for quantifying the concentration ratios of chemical elements in nanoparticles is X-ray photoelectron spectroscopy (XPS).[46,47] By taking advantage of energy tunable synchrotron radiation, depth-profiling of concentration ratios can be achieved. This is done by changing the photon energy, which changes the kinetic energy of the photo-emitted electrons and, therefore, the probing depth.[48] Previous XPS depth-profiles on UCNPs have provided evidence for $NaYF_4$@$NaGdF_4$ core@shell structures,[49] different chemical speciation of Yb^{3+} at the surface,[50] and non-uniform depth distribution of sensitizer ions.[51] Most previous XPS studies of UCNPs have used the soft X-ray energy range (<2000 eV), which limits the sampling depth to a few nanometers. Less commonly used is depth-profiling with tender X-ray photoemission ($h\nu \approx$ 2000 eV to 10 000 eV), commonly referred to as Hard X-ray Photoemission Spectroscopy, or HAXPES. HAXPES depth-profiling allows deeper probing into the nanoparticles and information depths ranging from ≈5 to 30 nm.[52] These information depths are ideally matched to typical UCNP radii, providing a unique opportunity to study dopant ion concentration profiles over the entire depth of interest. HAXPES also provides access to higher binding energy core levels, for example, the 3d core levels of Yb and Er. The 3d core levels of Yb and Er are better separated in binding energy than the 4d levels leading to simpler spectral analysis. This increased binding energy separation can be particularly useful for studying lanthanide dopants in UCNPs, where the identification and quantification of Er^{3+}, most commonly in concentrations of only ≈2%, has not been previously achieved with XPS. Another advantage to using the 3d core levels in the current study is their higher photoionization cross-sections in the tender X-ray range, compared to the 4d core levels. Here, in a proof-of-concept study, HAXPES combined with data simulation is used to determine depth-profiles of the concentration ratio of Er^{3+} to Yb^{3+} ($[Er^{3+}]/[Yb^{3+}]$) for three different types of $NaYF_4$-based core and core@shell UCNPs prepared with two different synthetic methods. Models for the depth distribution of $[Er^{3+}]/[Yb^{3+}]$ in the three types of particles are constructed by comparing the experimental data to simulated data produced using the simulation of electron spectra for surface analysis (SESSA) program.[53] Inductively coupled plasma-optical emission spectroscopy (ICP-OES) measurements were utilized to translate the distribution of relative dopant ion concentrations obtained by modeling the HAXPES data into mol % distributions of the individual lanthanide dopant ions throughout the UCNPs. The range of particle sizes and architectures used in this study demonstrates the potential of this approach as a powerful, general method for determining dopant ion concentration profiles in UCNPs. This enables correlations between the different spatial distributions of the lanthanide ions in the UCNPs and their luminescent properties to be established.

2. Results

To demonstrate the ability of HAXPES depth-profiling with tender X-rays for characterizing dopant ion distributions in lanthanide-based UCNPs, we prepared three different samples (labeled A, B, and C), that varied in Yb^{3+} and Er^{3+} dopant distribution and crystal phase. The corresponding synthesis procedures and the targeted UCNPs architectures are presented in **Figure 1**. As schematically illustrated, the synthesis method of sample A targets hexagonal phase UCNP with homogeneously distributed Yb^{3+} and Er^{3+} and the synthesis method for sample B targets a core@shell UCNP with Yb^{3+} confined exclusively to the core and Er^{3+} to the shell. The synthesis method used for sample C, on the other hand, aims at producing cubic phase UCNPs. The three different types of $NaYF_4$:Er^{3+},Yb^{3+} UCNPs examined were all synthesized by thermal decomposition processes. $XCl_3 \cdot 6H_2O$ precursors were used for samples A and B while trifluoroacetate precursors were used in the case of sample C. Sample A was made in such a way that homogeneous dopant concentrations of 2% Er^{3+} and 20% Yb^{3+} throughout the particle are likely. In the case of sample B, an active Yb-core@Er-shell structure was produced by first preparing core particles doped only with Yb^{3+}. These core particles were then used for the epitaxial growth of an Er^{3+} doped $NaYF_4$ shell. The reagent concentrations used aim at dopant concentrations of 20% Yb^{3+} in the core and 2% Er^{3+} in the shell of the UCNPs of sample B.

2.1. Structural Characterization

Transmission electron microscopy (TEM) images (**Figure 2**a,b) show that both $XCl_3 \cdot 6H_2O$ synthesized nanoparticles (Samples A and B) are hexagonal UCNP structures with narrow size distributions as have been previously reported.[38,39,54] The particle sizes of samples A and B are 48 ± 4 nm and

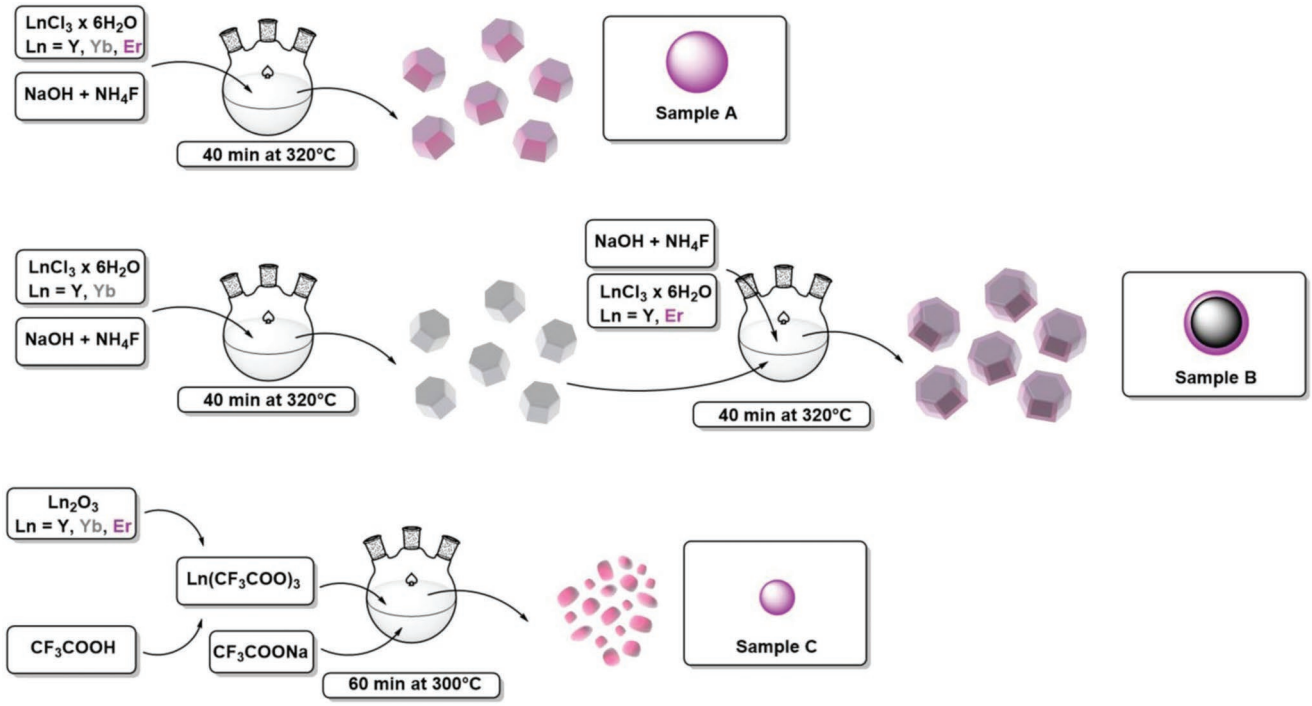

Figure 1. Synthesis procedures for the preparation of samples A, B, and C.

38 ± 2 nm, respectively. The shape and size distribution of the resulting UCNPs using trifluoroacetate precursors (Sample C) (Figure 2d) resemble those produced in the original synthesis by Boyer et al.[55] Here, particles with an inhomogeneous shape and higher polydispersity with an average diameter of 19 ± 11 nm were observed (Figure 1c,d). The X-ray diffraction (XRD) patterns (Figure 2e) show that samples A and B consist of pure hexagonal β-phase $NaYF_4$, while the host matrix of C is purely cubic (α-phase) $NaYF_4$.

2.2. Optical Properties

The optical properties of the oleate-stabilized UCNP samples A, B, and C were measured in cyclohexane under identical conditions (i.e., absorbance at the 980 nm excitation wavelength, excitation power density, spectrometer settings). As the ligand, the environment (e.g., the solvent, electrolyte, and pH), and the excitation power density are known to affect the photoluminescent properties of UCNPs, this enables a reasonable comparison.[23,56–58] The UCL spectra presented in **Figure 3**a show considerable differences in the red to green (R/G) ratios (**Table 1**) between UCNPs A, B, and C (also see Figure S1, Supporting Information where the emission is normalized to the green emission at 540 nm). In addition to other parameters like size, UCNP environment, and excitation power density,[54,59] the relative spectral contribution of the green (525 and 542 nm) and red (654 nm) bands to UCL depends on the crystal phase of the UCNP.[60] In the case of β-UCNPs (samples A and B), there is a smaller energy mismatch between the Yb^{3+} $^2F_{5/2}$ and Er^{3+} $^4I_{11/2}$ states than in α-UCNPs (sample C).[60] This results in a more efficient energy transfer to the Er^{3+} $^4I_{11/2}$ state and subsequent excitation to the $^4F_{7/2}$ state (a pathway for green or red emission, see Figure S7, Supporting Information) and less efficient relaxation into the $^4I_{13/2}$ state (a pathway for red emission). This can lead to a net gain in green emission for UCNPs in the β-phase compared to the α-phase.[60] In our case, the β-UCNPs (samples A and B) have an R/G ratio of 2 and 0.42, respectively, compared to the α-UCNPs (sample C) which have an R/G ratio of 4. Considering the two β-phase UCNPs in this study, samples A and B, there is a factor of 5 higher R/G ratio for sample A, with a homogenously distributed $[Er^{3+}]/[Yb^{3+}]$, compared to sample B, with a Yb-core@Yb,Er-shell@Er-shell structure. Time-resolved PL measurements recorded at emission wavelengths of 1010 nm (down-shifted Yb^{3+} luminescence (DSL)) (see Figure 3 and Table 1) reveal that confining Yb^{3+} to the core and reducing surface quenching of the excited Yb^{3+} states leads to an almost 4 times longer lifetime of the 1010 nm DSL in sample B compared to sample A as reported for many other UCNPs.[31,38] The DSL of Yb^{3+} at 1010 nm following excitation at 980 nm occurs due to the Stark splitting of the $^2F_{5/2} \rightarrow {}^2F_{7/2}$ Yb^{3+} manifold in the host matrix.[61] The longer lifetime of the excited Yb^{3+} state results in the observed longer lifetime of 542 nm (green Er^{3+} emission) of sample B compared to A since the rate of energy transfer from the excited Yb^{3+} to Er^{3+} is proportional to the amount of excited Yb^{3+}.[62] The similar lifetimes of the red Er^{3+} emission in both samples A and B are indicative of similar concentration quenching effects of the excited Er^{3+} ions. The observed emission characteristics of the three UCNP samples, including the lifetimes, are expected from the UCNP architectures and dopant ion distributions targeted for this study and confirmed by their structural characterization. However, these structures may not represent the true, quantitative concentration profiles of the active lanthanide ions within the UCNPs.

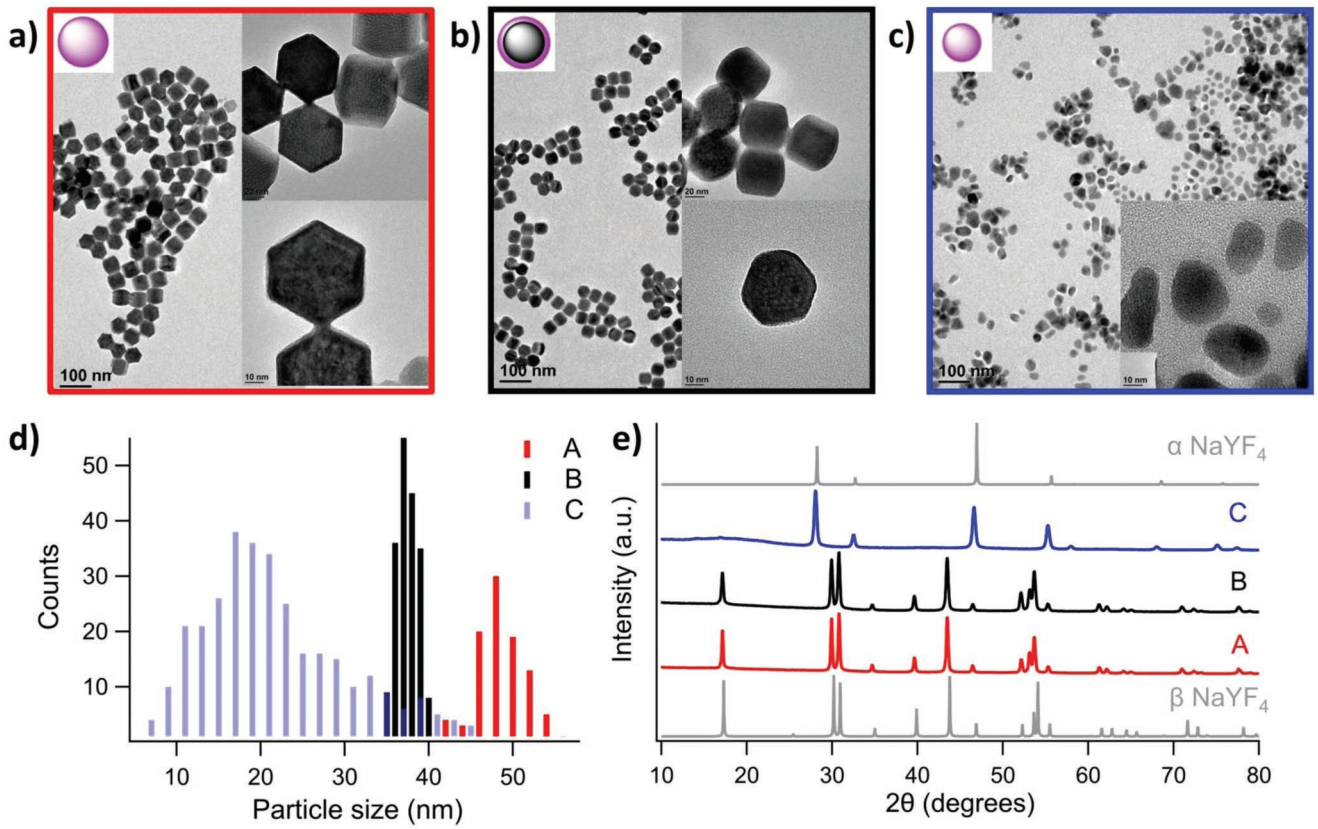

Figure 2. Transmission electron microscopy (TEM) images of a) core only $NaYF_4$:Er^{3+},Yb^{3+} UCNPs made via thermal decomposition with $XCl_3.6H_2O$ precursors (sample A). b) $NaYF_4$ core(Yb)@shell(Er) UCNPs made via thermal decomposition with $XCl_3.6H_2O$ precursors (sample B). c) $NaYF_4$:Er^{3+},Yb^{3+} UCNPs made via thermal decomposition with trifluoroacetate precursors (sample C). The insets on (a) and (b) show the nanoparticle shape inferred from the TEM images. d) Size distribution and e) the X-ray diffraction (XRD) patterns of UCNP samples A, B, and C with references to alpha (α) and beta (β) phase $NaYF_4$.

2.3. Depth-Profiling HAXPES

To obtain deeper insight into the actual sensitizer and activator dopant ion concentration distribution in samples A, B, and C, we performed depth-profile analyses of the Yb^{3+} and Er^{3+} ion concentration ratio ($[Er^{3+}]/[Yb^{3+}]$) with HAXPES combined with simulations using the SESSA software package. The Er $3d_{5/2}$ and Yb $3d_{5/2}$ HAXPES spectra were measured using a series of photon energies between 2000 and 6000 eV (**Figure 4**a,b for spectra from sample A; see Supporting Information for spectra from samples B and C). As noted in the introduction, the 3d core levels of these lanthanide ions are ideal for quantifying the ratio of activator and sensitizer ions due to their binding energy separation and increased photoionization cross-sections compared to the 4d core levels. For sample A, data were not acquired at 6000 eV photon energy, and 5000 eV was the highest photon energy used. Also, a photon energy of 2970 eV was used instead of 3000 eV for all samples to avoid an Auger peak overlapping with the Er $3d_{5/2}$. In principle, the 4d core levels could also be used for depth-profiling, but their overlap with satellite features from the lanthanides and the Y 3d (see Supporting Information) makes this approach more challenging, particularly for low Er^{3+} doping concentrations.

The Er $3d_{5/2}$ spectra are consistent with previous observations for Er^{3+} with the main feature centered at 1410 eV and a satellite (energy loss) feature at 1419 eV.[63] The Yb $3d_{5/2}$ spectra contain the main Yb^{3+} feature at 1524–1536 eV, a plasmon satellite (energy loss) peak at 1546 eV, and a small contribution of Yb^{2+} at 1520 eV for sample A.[64–67] Additional core levels are shown in the Supporting Information. The contribution of Yb^{2+} in sample A to the total Yb $3d_{5/2}$ signal is at most 4%. This Yb^{2+} feature is only present at higher photon energies, implying that the concentration of Yb^{2+} is higher in the core of the nanoparticle. This small amount of Yb^{2+} does not originate from beam damage induced by long-time exposure to the X-rays. This is because an increase in the Yb^{2+} peak intensity was not observed while acquiring the data using sequential scans at the same photon energy. Moreover, the 2003 eV photon energy spectra, where Yb^{2+} is not observed, were recorded after the 2970 eV spectra implying that the Yb^{2+} was already present in the core of the UCNPs and not induced by the X-ray beam. This conclusion is further supported by the observation of Yb^{2+} solely in sample A; samples B and C would also be susceptible to beam damage if it occurred. Note that for the concentration ratios discussed in the next section the areas of all the features (main Yb^{3+} peak, satellites, and Yb^{2+} peak) present in the Yb $3d_{5/2}$ spectra were included for quantification.

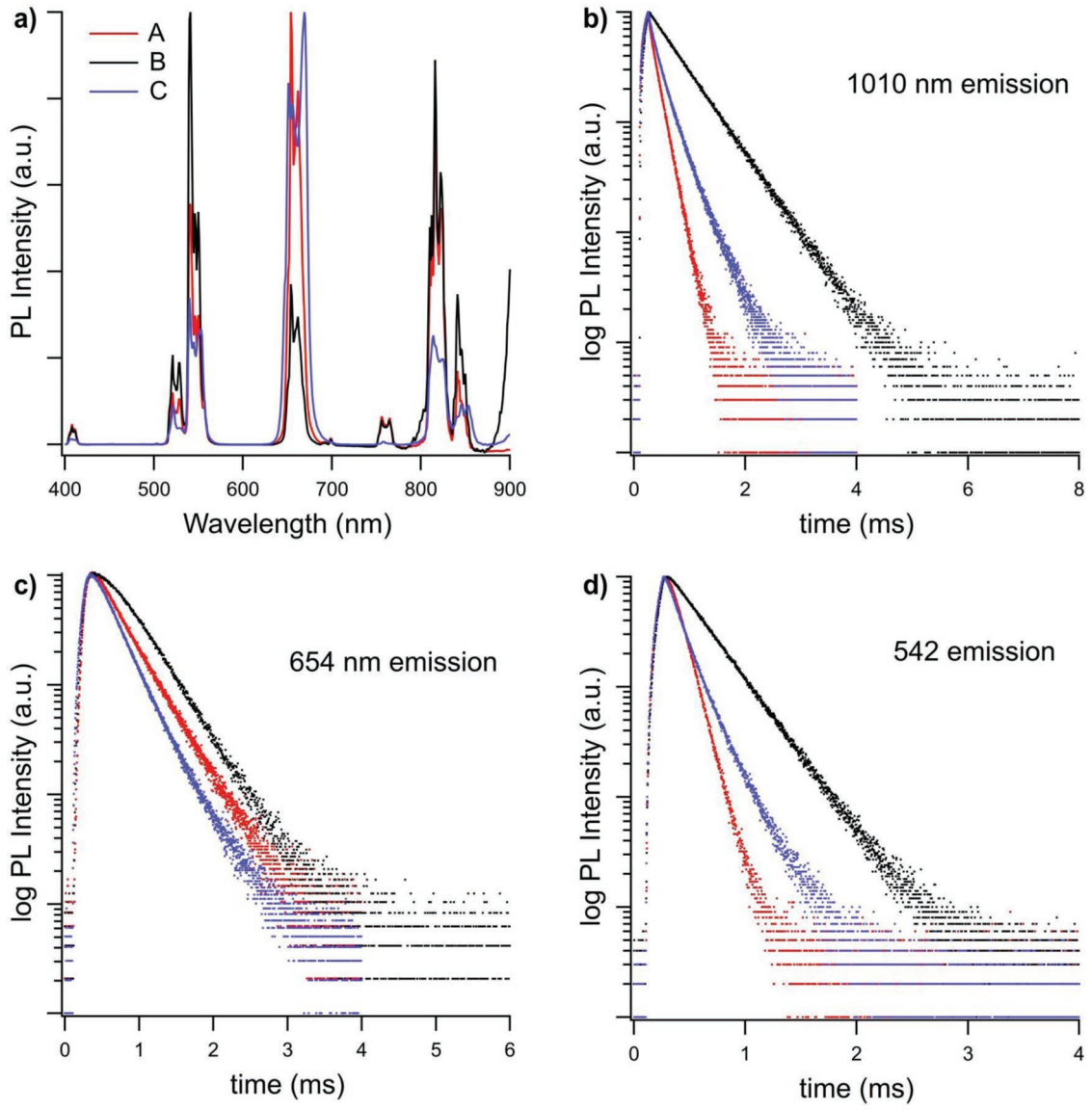

Figure 3. a) Photoluminescence (PL) spectra of the three UCNP samples A, B, and C normalized to the highest emission intensity of each spectrum. PL decay curves under 980 nm excitation at b) 1010 nm (downshifted Yb^{3+} emission), c) 654 nm (red Er^{3+} UCL), d) 542 nm (green Er^{3+} UCL).

The increasing kinetic energy of the photoelectrons emitted from the 3d core levels with increasing photon energy results in increasing probe depths.[48,68,69] Figure 4c shows how the intensity of photoelectrons from the 3d core levels should vary with depth into the nanoparticle at two different photoelectron kinetic energies, 600 eV (photon energy of ≈2003 eV) and 4600 eV (photon energy of ≈6000 eV).[70] The data taken with the 2003 eV photon energy is quite surface-sensitive with probe depths (defined as 3λ, where λ is the inelastic mean free path) of ≈5 nm, while the data taken with 6000 eV photon energy (3λ = ≈26.5 nm) has probe depths equal to approximately half of the diameter of the nanoparticle. The $[Er^{3+}]/[Yb^{3+}]$ ratio, calculated from the areas of the core levels (after subtracting Shirley backgrounds and correcting for photoionization cross-sections), is displayed in Figure 4d. There are clear differences between the three samples. The expected value for the $[Er^{3+}]/[Yb^{3+}]$ ratio of a UCNP containing a dopant ion concentration ratio equal to that of the reaction mixture (2% Er and 20% Yb) is 0.1. Sample A shows approximately the expected 0.1 concentration ratio at all depths, confirming that it is composed of core-only UCNPs with a homogeneous distribution of the

Table 1. Red to green ratios derived from the integrated areas of the red and green emission bands and lifetimes obtained from the PL decay curves recorded at 1010, 654, and 542 nm and fitted with mono-exponential decays.

Sample	Red to green ratio	Lifetime at 1010 nm [µs]	Lifetime at 654 nm [µs]	Lifetime at 542 nm [µs]
A	2.02	151	326	110
B	0.42	586	358	313
C	3.90	235	293	163

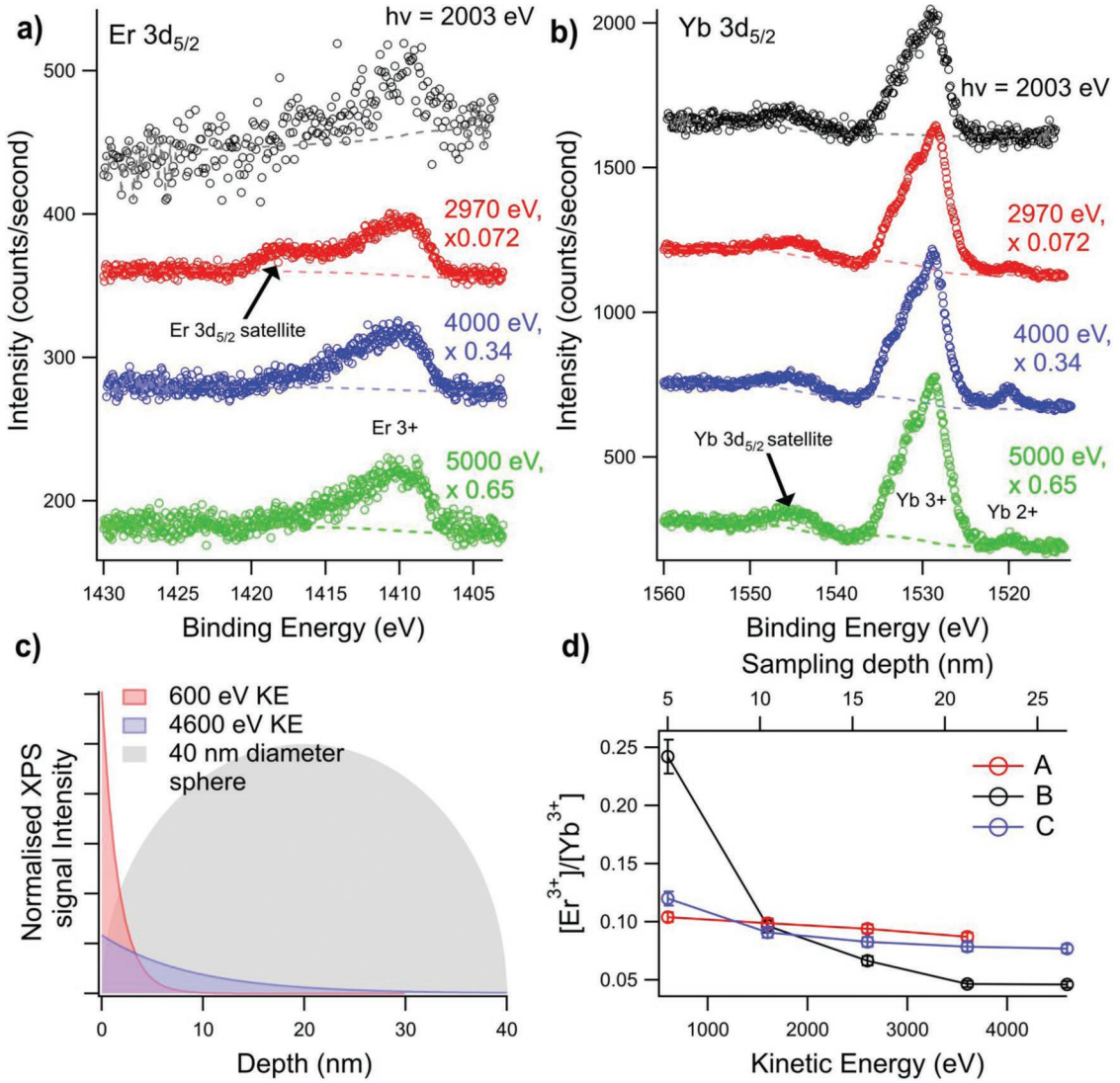

Figure 4. Hard X-ray photoemission spectroscopy (HAXPES) spectra of the a) Er $3d_{5/2}$ and b) Yb $3d_{5/2}$ core levels from sample A at four different photon energies, both are scaled so that the Er $3d_{5/2}$ area is constant at each photon energy for presentation. The main features in both spectra are labeled and the fitted Shirley backgrounds are shown with dashed lines. The photon energy of each spectrum and the scaling factor are also shown (no scaling factor is shown at 2003 eV because this data is not scaled). c) The HAXPES signal intensity profiles of 600 eV KE photoelectrons (red) and 4600 eV photoelectrons (blue), which are representative of photoelectrons from the Er 3d core level at 2003 and 6000 eV photon energy. The integrated area under the red and blue curves is normalized by their total area to give an area of 1, to make comparison of surface sensitivity simpler. d) The concentration ratio of the activator to sensitizer ions ($[Er^{3+}]/[Yb^{3+}]$) for samples A, B, and C as a function of kinetic energy (sampling depth). The concentration ratios are calculated from the extracted $3d_{5/2}$ core level areas of Er and Yb and corrected for the respective photoionization cross-sections. Errors in concentration ratios are calculated by changing the background fit to the spectra.

dopant ion concentration ratios. This $[Er^{3+}]/[Yb^{3+}]$ is, however, also consistent with Er^{3+} and Yb^{3+} dopant ion concentrations other than 2% and 20%, respectively, as long as their ratio is equal to 0.1 (e.g., a homogeneous distribution of 1% Er^{3+} and 10% Yb^{3+} is also consistent with the data). This will be discussed below in further detail. Sample B on the other hand, is clearly not a core-only nanoparticle, as there is an enhancement of $[Er^{3+}]/[Yb^{3+}]$ at the particle surface, and the concentration ratio drops below 0.1 for increased probing depths. Sample C displays concentration ratios close to 0.1 throughout the nanoparticle, but with $[Er^{3+}]/[Yb^{3+}]$ slightly above 0.1 at the surface and its depletion deeper in the nanoparticle.

2.4. SESSA Simulations

To gain further insight into the distribution of $[Er^{3+}]/[Yb^{3+}]$ within the particles, SESSA simulations were carried out using model nanoparticles with various $[Er^{3+}]/[Yb^{3+}]$ distributions and the results were compared to the experimentally determined distribution of $[Er^{3+}]/[Yb^{3+}]$ found via HAXPES. Details of the parameters used for the SESSA simulations are included in the Supporting Information. Our HAXPES measurements average over many particles that can have any orientation on the substrate. This means that we average over any particle property that may have an orientational dependence. In particular,

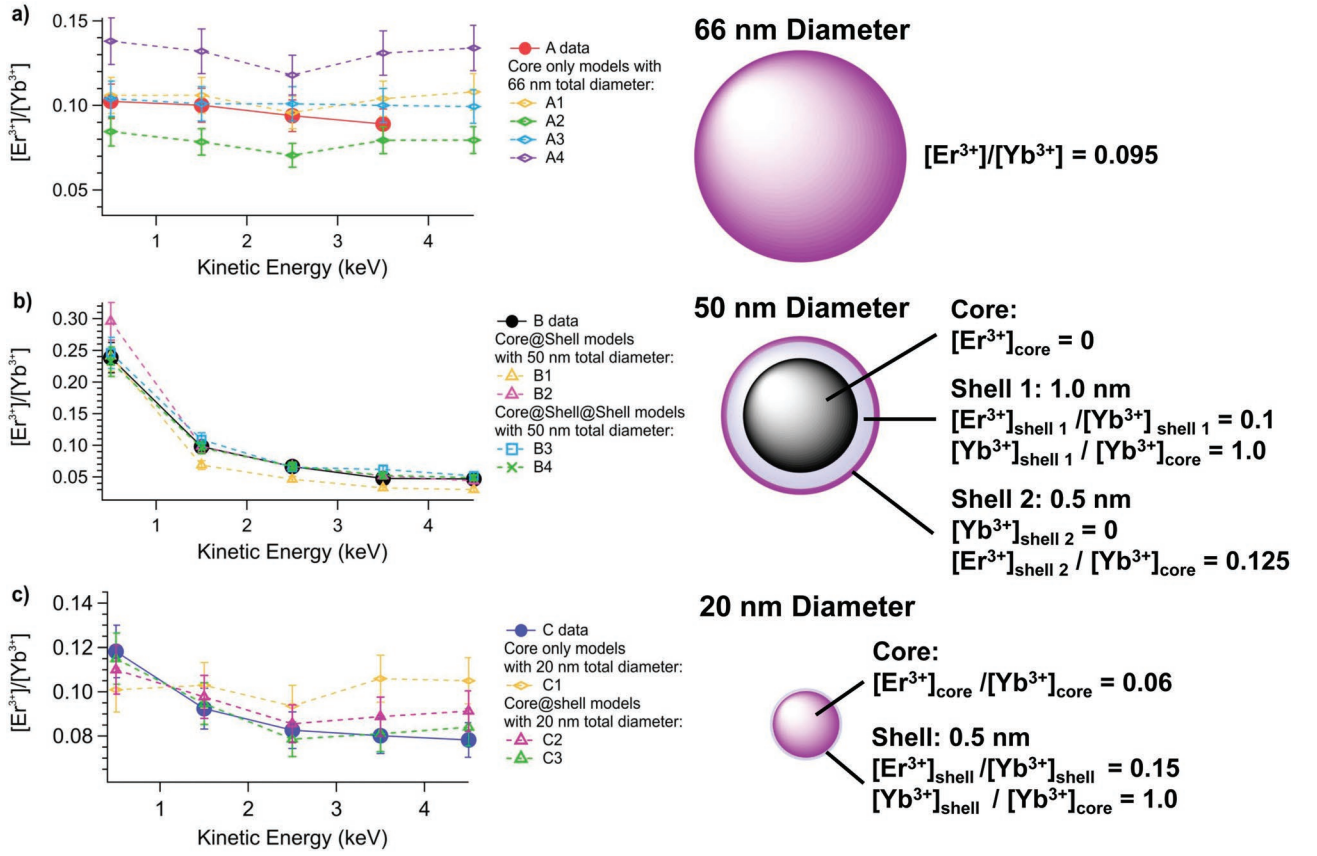

Figure 5. Simulation results of the $[Er^{3+}]/[Yb^{3+}]$ concentration ratio calculated over a range of kinetic energies for different core@shell structures plotted against the experimental data from samples A, B, and C in (a), (b), and (c) respectively. See Table S4, Supporting Information, for details on the UCNP architectures used for the simulated data, A1 to A3, B1 to B3, and C1 to C4, as well as additional simulations that are not shown. On the right are schematics of the models that best fit the data for each sample. The associated error bars originate from uncertainties in material properties used in the calculations (see Supporting Information).

variations in shell thicknesses on different crystal facets as a result of facet-dependent shell growth kinetics are averaged out. For this reason, spherically shaped particles are an appropriate shape for simulating our data, and our dopant ion concentration ratios should be interpreted as being averaged over all particle orientations and, therefore, all possible shell thicknesses in the case of Sample B. Spherical models with diameters of 66, 50, and 20 nm were used for samples A, B, and C, respectively. These diameters were chosen to best represent the total volume of the particles determined from the TEM images as stated above. For core-only structures, a simple spherical model with a constant stoichiometry was used to calculate expected Er $3d_{5/2}$ and Yb $3d_{5/2}$ signal intensity ratios at each kinetic energy. Then the $[Er^{3+}]/[Yb^{3+}]$ ratio for the model particles was varied and the simulations repeated for each kinetic energy. The results of the simulations were then compared to the experimental data over the full kinetic energy range. To simulate the data for core@shell(s) structures, layered spheres with shells of different thicknesses (1 to 8 nm) and with different $[Er^{3+}]/[Yb^{3+}]$ ratios were simulated for all kinetic energies measured. This was done by fixing the $[Er^{3+}]/[Yb^{3+}]$ ratio in the core and shells of the particle at specific values, while varying the core diameter and shell thicknesses, keeping the total particle diameter constant. Simulated Er $3d_{5/2}$ and Yb $3d_{5/2}$ signal intensity ratios were then compared to the experimentally measured ratios over the entire kinetic energy measured. We then changed the values of the $[Er^{3+}]/[Yb^{3+}]$ in the core and shells of the particle and simulated the Er $3d_{5/2}$ and Yb $3d_{5/2}$ signal intensity ratios again by varying the core diameter and shell thicknesses and compared these new simulated values to the measured data over the measured kinetic energy range. This procedure continued until a satisfactory match was found which we defined as being within one standard deviation of the experimental data at each kinetic energy (see Experimental section).

The SESSA simulations that best match the results for sample A are those for a core-only $NaYF_4:Er^{3+},Yb^{3+}$ nanoparticle with a homogeneously distributed $[Er^{3+}]/[Yb^{3+}]$ concentration ratio equalling 0.095, shown in **Figure 5**a. For core@shell UCNPs the trend in $[Er^{3+}]/[Yb^{3+}]$ as a function of depth into the UCNP (Figure 5b) depends on the relative concentrations of the dopant ions between the core and the shell in addition to their relative concentrations within the core and shell. For example, consider two samples of UCNPs, both with $([Er^{3+}]/[Yb^{3+}])_{shell} = 0.1$ in the shell and $([Er^{3+}]/[Yb^{3+}])_{core} = 0.5$ in the core, but where the relative concentrations of Yb^{3+} in the shell and the core, $[Yb^{3+}]_{shell}/[Yb^{3+}]_{core}$ differ by a factor of 100. For the case where $[Yb^{3+}]_{shell}/[Yb^{3+}]_{core}$ is large (i.e., small $[Yb^{3+}]_{core}$ relative to $[Yb^{3+}]_{shell}$), $[Er^{3+}]/[Yb^{3+}]$ would start near 0.1

at low KE, and increase only slightly with increasing KE. In the case where $[Yb^{3+}]_{shell}/[Yb^{3+}]_{core}$ is small, $[Er^{3+}]/[Yb^{3+}]$ would also start near 0.1 at low KE but increase more dramatically with increasing KE. Therefore we must designate one relative dopant ion concentration between the core and shell(s) to simulate the data. We have chosen to use the Yb^{3+} concentration in the core, $[Yb^{3+}]_{core}$ for our simulations. For sample B, the best match to the data was found for a UCNP with two shell layers and a core containing only Yb^{3+}. A satisfactory fit to the data for sample B could not be made using a model with only one shell. In the best-fit model (B4 in Figure 5b), the particle's outermost shell is 0.5 nm thick and doped with only Er^{3+} with a concentration that is 0.125 times the Yb^{3+} in the core. The second shell lying between the outermost shell and the core is co-doped with a $[Er^{3+}]/[Yb^{3+}]$ of 0.1 and a thickness of 1.0 nm. The Yb^{3+} concentration in this inter-layer is 1.0 times the Yb^{3+} concentration in the core. Included in Figure 5b (orange, B1) are the modeled concentration ratio profiles of a pure Yb^{3+} core@pure Er^{3+} shell structure without a co-doped inter-layer. The concentration of Er^{3+} in the shell is 0.1 times the concentration of Yb^{3+} in the core with a shell thickness of 0.8 nm. Also included in Figure 5b (blue, B3) is a second structure with a co-doped inter-layer. In this case, the inter-layer has a $[Er^{3+}]/[Yb^{3+}]$ ratio of 0.1, the same as the better fitting model B4, but with a thickness that is 1.5 times the thickness in the B4 model. The concentration of Er^{3+} in the outer shell is 0.8 times the concentration in the outer shell of model B4. For the low concentrations of Er^{3+} found in these UCNPs, this difference in dopant ion concentration ratios would translate into less than one mol% of Er^{3+}. Comparison of models B3 and B4, therefore, shows how sensitive the modeling is to changes in the UCNP architecture (see Supporting Information for comparison to further simulations using other model particles).

The broader size distribution of the UCNPs in sample C decreases the accuracy of the match between the ion distributions found with the SESSA simulations and the true ion distributions in the UCNPs. However, there is evidence for a small enhancement of the $[Er^{3+}]/[Yb^{3+}]$ ratio at the particle surface and a concomitant depletion in the interior. The simulated data that best matches the experimental data is for a 20 nm diameter spherical nanoparticle with a 0.5 nm thick shell with Er^{3+} at a concentration of 0.15 times the concentration of Yb^{3+}, and a co-doped core with a $[Er^{3+}]/[Yb^{3+}]$ of 0.06. Further simulations can be found in the Supporting Information along with a table detailing the various UCNP architectures used for the simulations. The right-hand side of Figure 5 schematically shows the best-fit concentration ratios of the dopant ions for all three particle sizes and architectures.

2.5. Inductively Coupled Plasma-Optical Emission Spectroscopy (ICP-OES)

ICP-OES is a powerful analytical ensemble technique for the detection and quantification of chemical constituents and was therefore used to determine the chemical composition of the three types of UCNPs. The results of our ICP-OES measurements indicated that Sample A consists of 1.85 mol% Er^{3+}, 19.35 mol% Yb^{3+} and 78.79 mol% Y^{3+}, Sample B 0.37 mol% Er^{3+}, 16.12 mol% Yb^{3+} and 83.51 mol% Y^{3+}, and Sample C has 1.60 mol% Er^{3+}, 14.35 mol% Yb^{3+} and 84.04 mol% Y^{3+}. Note that these values are averaged over the entire volume of the UCNPs and over a large number of particles and do not provide information about the distribution of the dopant ions within the UCNPs or in individual UCNPs. Below, these values will be used to calibrate the dopant ion ratios obtained from the SESSA simulations to provide dopant ion concentration profiles in the three types of UCNPs on a mol % basis.

3. Discussion

3.1. Combining HAXPES Depth-Profiling, SESSA Simulations, and ICP-OES to Determine Dopant Ion Distributions

In Figure 5, the dopant ion concentration ratios determined from the best-fits to the HAXPES depth-profiling data are all relative to $[Yb^{3+}]_{core}$. Once $[Yb^{3+}]_{core}$ is determined on a mol % basis, all other dopant ion concentrations and their distributions in the UCNPs can be determined on a mol % basis. $[Yb^{3+}]_{core}$ can be calculated from the total amount of Yb^{3+} measured by ICP-OES, and the relative amounts of Yb^{3+} in the shells and cores of the samples, along with the fractional volume of the shells and cores, determined from the HAXPES simulations of the dopant ion concentration ratios (see Supporting Information for an example calculation using sample B). Effectively, the ICP-OES measurement of $[Yb^{3+}]$ is used as a calibration for the HAXPES dopant ion distribution profiles. Determining $[Yb^{3+}]_{core}$ in this way also allows us to calculate the total amount of Er^{3+} in the model UCNP samples by integrating $[Er^{3+}]$ over the volume of the model UCNPs. These values can then be compared to the amount of Er^{3+} measured by ICP-OES (see Supporting Information) to check the accuracy of our model UCNPs. **Figure 6** shows the distribution of Er^{3+} and Yb^{3+} dopant ion distributions resulting from this analysis, and Table S5, Supporting Information, provides the comparison of the values for the total mol % of Er^{3+} in the UCNPs (obtained by integrating the Er^{3+} distributions from this analysis over the volume of the particles) to that measured with ICP-OES. In all cases, the amounts of $[Er^{3+}]$ calculated from the simulated HAXPES data are within a fraction of a mol percent of the measured amount from ICP-OES. This is well within the expected accuracy of XPS measurements of chemical compositions.[71]

3.2. Dopant Ion Distributions

The concentrations and distributions of $[Er^{3+}]$ and $[Yb^{3+}]$ for sample A are very close to what was targeted with the synthesis, 2% and 20% respectively. Similarly, our results are consistent with the targeted homogeneous distribution of both dopants throughout the UCNPs of sample A.

For sample B, the core and outer shell compositions are also close to the values aimed at with the synthesis (20% Yb^{3+} and 2% Er^{3+} doping, respectively), however, the core of the particles have Yb^{3+} concentrations somewhat below the targeted values. The reason for this is unclear, but may be

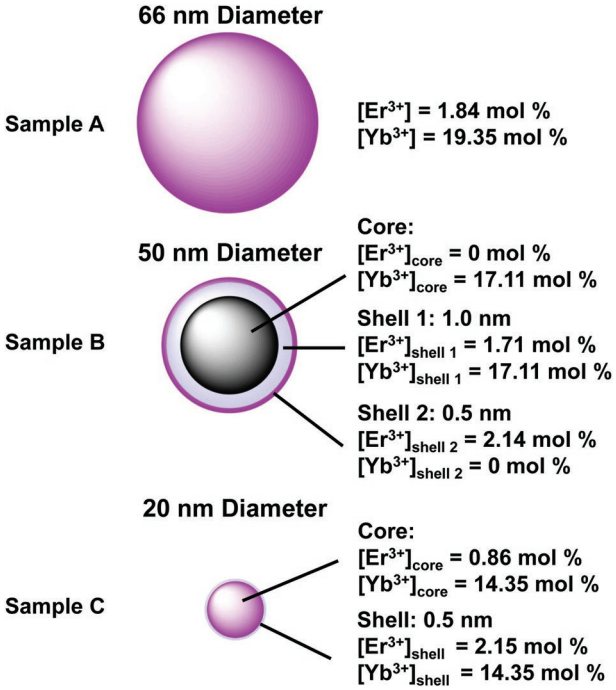

Figure 6. Er^{3+} and Yb^{3+} dopant ion distributions in the three types of UCNPs investigated.

indicative of synthesis to synthesis variation. Additionally, there may have been differences in the dopant concentrations between large and small nanoparticles produced during the synthesis. These smaller nanoparticles were separated from the β-UCNPs of sample B after synthesis and not further studied (see Figure S6, Supporting Information), which may account for the missing material. Model nanoparticles of sample B indicate a co-doped inter-layer between the core and outer shell of the nanoparticle. This inter-layer may be due to diffusion and intermixing of the lanthanide ions between the layers during the synthesis of the Yb-core@Er-shell nanoparticles and/or core dissolution and recrystallization during the shelling step of the synthesis.[45] In reality, the boundaries between this inter-layer and the core and shell of the UCNPs are likely not abrupt. Instead, the inter-layer between the core and shell of the UCNPs likely has intermixed regions with varying $[Er^{3+}]/[Yb^{3+}]$ that extend into both the core and the shell. Recent evidence for intermixed layers in UCNPs has been provided by energy-dispersive X-ray spectroscopy line profiles in a transmission electron microscope.[44] While Hudry et al. provided evidence for intermixing in individual UCNPs, our depth-profiling analysis with HAXPES gives complementary evidence for intermixing averaged over an ensemble of UCNPs. Since the optical properties are typically measured over an ensemble of UCNPs, although single particle studies do exist,[38,72–75] averaged depth-profiles can be more readily correlated with optical measurements. In addition, core-level HAXPES is a more direct method to quantitatively determine chemical speciation, for example the small amount of Yb^{2+} observed in the UCNP particle core of sample A.

The model UCNPs for sample C indicates an inhomogeneous distribution of Er^{3+} throughout the particles and dopant ion concentrations below the values targeted with the synthesis. Interpretation of these results should be done cautiously, however, due to the broad size and shape distribution of the UCNPs in sample C. For example, smaller, Er^{3+}-rich nanoparticles could lead to an apparent surface enhancement of Er^{3+} in the HAXPES data which averages over all particle shapes and sizes. This reflects a limitation of our approach which is best applied to ensembles of UCNP with uniform sizes, shapes, and dopant ion distributions among the UCNPs making up the ensemble.

Our results demonstrate the ability to combine HAXPES depth-profiling, ICP-OES measurements, and SESSA simulations of the HAXPES data to provide a detailed, quantitative description of the distribution of Yb^{3+} and Er^{3+} ions in $NaYF_4$-based UCNPs. In particular, we have derived direct evidence of an intermixed layer in core@shell UCNPs synthesized using standard shell-forming procedures. Such intermixed layers have been previously inferred indirectly from optical measurements.[31] The presence of such intermixed layers can affect the optical properties of the UCNPs. For example, since the concentration of Er^{3+} is lower in the intermixed layer than in the shell, cross-relaxation should be reduced in the interlayer compared to the shell and the diminished concentration of Yb^{3+} in the intermixed layer could lead to a reduced rate of energy transfer from Yb^{3+} to Er^{3+}, assuming that the Yb^{3+} ions in closest proximity to the Er^{3+} are most effective in transferring their energy.

4. Conclusion and Outlook

In conclusion, we demonstrated that HAXPES depth-profiling, which is ideally matched to the typical sizes of UCNPs, when combined with SESSA simulations of the data, is a powerful method for investigating the Er^{3+} and Yb^{3+} concentration profiles in UCNPs. Using three types of $NaYF_4$:Er^{3+}, Yb^{3+} UCNPs with different particle sizes and architectures, we have shown that this approach is also quite general and applicable to a broad range of nanoparticle sizes and types. We have also pointed to limitations, in that the data is more readily interpreted for ensembles of nanoparticles with uniform size, shape, and dopant ion distributions. In addition, using tender X-rays allows measuring the Er and Yb 3d core levels which have larger photoionization cross-sections and are better separated in binding energy compared to their 4d counterparts making them particularly well suited for dopant ion concentration profile analysis of UCNPs containing only 2% of Er^{3+}. By comparing simulated $[Er^{3+}]/[Yb^{3+}]$ concentration profiles to the experimentally measured ones, models for the distribution of Er^{3+} and Yb^{3+} throughout the UCNPs were provided. These models suggest differences in the ion distributions between various synthesis methods, as well as inter-diffusion of lanthanide ions in a Yb-core@Er-shell structure, resulting in a co-doped interlayer and a Yb-core@Yb,Er-shell@Er-shell structure. The differences in the $[Er^{3+}]/[Yb^{3+}]$ distributions can be correlated with the observed differences in the optical properties of the UCNPs, in particular the different R/G ratios and the emission lifetimes.

Having demonstrated the power of depth-profiling HAXPES combined with simulations to extract the relative dopant concentration distribution in UCNPs, in the future we plan to more

systematically investigate different types of UCNP structures, targeting a broad range of particle sizes, shell thicknesses, and chemical compositions. These structures will include different particle architectures, varying in dopant ion concentrations and distributions. We plan to further correlate the results of depth-profiling HAXPES with mechanistic studies of the luminescence features of these UCNPs and the assessment of different synthetic approaches. Such studies will deepen the understanding of the precise role of intermixed layers on the UCNPs' optical properties and provide a handle to further optimize and fine-tune UCNP synthesis.

5. Experimental Section

Synthesis of Core-only β-phase UCNPs (Sample A): Co-doped, oleate-capped, hexagonal-phase $NaYF_4$:20%Yb^{3+},2%Er^{3+} UCNPs were synthesized following the procedure reported by Wilhelm et al.[54] Briefly, $YCl_3{\cdot}6H_2O$ (1183.10 mg, 3.90 mmol), $YbCl_3{\cdot}6H_2O$ (387.50 mg, 1 mmol), and $ErCl_3{\cdot}6H_2O$ (38.17 mg, 0.10 mmol) were dissolved in 15 mL of methanol by sonication and subsequently added to a mixture of oleic acid (OA, 40 mL) and 1-octadecene (ODE, 75 mL) in a 250 mL three-necked flask. The stirred reaction mixture was then heated to 150 °C under argon flow for 30 min. Then vacuum was applied for a further 30 min at 150 °C to remove remaining water. The lanthanide precursor-containing reaction mixture was then cooled down to room temperature under a constant argon flow. Subsequently, a methanolic solution (30 mL) containing NaOH (500 mg, 12.5 mmol) and NH_4F (740 mg, 20 mmol) was added, and the resulting suspension was heated to 120 °C for 30 min to remove excess methanol. The reaction mixture was heated to 325 °C under reflux while applying a gentle flow of argon and kept at this temperature for 40 min. Then the reaction mixture was cooled down to room temperature. The resulting UCNPs were purified following the literature procedure.[54] Finally, the particles were dispersed in cyclohexane and stored at 4 °C.

Synthesis of Core-Shell β-Phase UCNPs (Sample B): The synthesis of core@shell oleate-capped $NaYF_4$:Yb^{3+}@$NaYF_4$:Er^{3+} was performed in two steps. First, the core $NaYF_4$:Yb^{3+} was synthesized according to the procedure described above using $YCl_3{\cdot}6H_2O$ (1214.20 mg, 4.0 mmol) and $YbCl_3{\cdot}6H_2O$ (387.50 mg, 1 mmol). After purification, the cores were used as seeds for the shell growth. Briefly, the shell precursors, $YCl_3{\cdot}6H_2O$ (201.55 mg, 0.66 mmol) and $ErCl_3{\cdot}6H2O$ (5.38 mg, 0.01 mmol), were dissolved in 20 mL OA and 37 mL ODE at 160 °C. After cooling to 80 °C, 40.2 mg core particles were added to the reaction mixture and the temperature was maintained at 80 °C to remove cyclohexane. Then, the temperature was lowered to 50 °C and methanolic solutions of NH_4F (100.44 mg, 2.71 mmol) and NaOH (69.8 mg, 1.74 mmol) were added. The reaction mixture was heated to 325 °C under reflux while applying a gentle flow of argon and kept at this temperature for 40 min. Then the reaction mixture was cooled down to room temperature. The resulting UCNPs were purified following a literature procedure.[54] Separation of the smaller particles from the desired core-shell nanoparticles was achieved by centrifugation of the particle dispersion in cyclohexane for 20 min at 10 000 rpm (13 639 rcf). Finally, the particles were dispersed in cyclohexane and stored at 4 °C.

Synthesis of α-Phase UCNPs (Sample C): The α-phase UCNPs were synthesized following the procedure reported by Boyer et al.[55] 9.6 mg (0.025 mmol) of Er_2O_3, 98.5 mg (0.25 mmol) of Yb_2O_3, 220.2 mg (0.975 mmol) Y_2O_3 were dissolved in 10 mL of 50% aqueous trifluoroacetic acid at 80 °C, then the residual water and acid were slowly evaporated at 50 °C before adding 0.34 g of sodium trifluoroacetate (98%), 20 mL octadecene (90%), and 20 mL oleic acid (90%). This mixture was slowly heated to 100 °C under vacuum whilst stirring for 30 min, and periodically purging with Ar gas. The mixture was then heated to 300 °C at a rate of 10 °C min^{-1} and kept at 300 °C for 1 h. The mixture was cooled to room temperature and the nanoparticles precipitated by adding a 1:4 hexane: acetone mixture. The nanoparticles were retrieved by centrifuging at 3000 rpm and washing with ethanol 3 times, drying under a vacuum in-between. The final nanoparticles, with oleic acid ligands, were dispersed in hexane.

Ligand Removal of $NaYF_4$:Yb^{3+},Er^{3+}—Ligand-Free $NaYF_4$:Yb^{3+},Er^{3+} UCNPs: Ligand-free $NaYF_4$:Yb^{3+},Er^{3+} were synthesized according to the procedure reported by Bogdan et al.[76] with some modifications. Briefly, oleate-capped UCNPs (100 mg) were isolated via centrifugation (30 min, 10 000 rpm) and dispersed in a 10 mL aqueous HCl (0.5 M) solution. Removal of oleate ligands was performed in an ultrasonic bath for 1 h at room temperature. When the reaction was completed, the aqueous solution was extracted three times with diethyl ether to remove the oleate ligands from the aqueous phase. The UCNPs in the aqueous phase were collected by centrifugation (30 min, 10 000 rpm) and washed twice with milliQ water. Finally, the particles were redispersed in water (c = 10 mg mL^{-1}) and stored at 4 °C. This ligand removal procedure was performed on samples A and B.

Transmission Electron Microscopy: Transmission electron microscopy (TEM) was performed on a CM12 Philipps with a 120 kV electron beam equipped with a supertwin objective lens and Gatan Orios CCD camera. For the TEM measurements, the UCNPs were deposited onto a copper grid by drop-casting.

X-Ray Diffraction: X-ray diffraction (XRD) patterns were collected using a Rigaku Ultima IV diffractometer (Rigaku, Tokyo, Japan) in a range of 10–80°/2θ with Cu Kα radiation (λ = 0.15406 nm). The acceleration voltage was 40 kV and the current was 40 mA. The scanning step was 0.2°/2θ with a counting time of 4 s per step.

Optical Characterization: Spectrally resolved UCL measurements were carried out on an Edinburgh Instruments Model FLS980-xD2-stm spectrofluorometer equipped with an 8 W, 978 nm laser diode. The emission wavelength range was set to 400–900 nm and a slit width of the emission monochromator of 5 µm was used. The red-to-green intensity ratios were derived from the integrated red and green Er^{3+} UCL bands.

Luminescence decay measurements were carried out on an Edinburgh Instruments Model FLS980-xD2-stm spectrofluorometer equipped with an electrically pulsed, 8 W, 978 nm laser diode (long square pulses, pulse width of 150 µs). The decay kinetics were recorded at 542 and 654 nm (Er-UCL) as well as at 1010 nm (downshifted luminescence (DSL) of Yb) with a red-sensitive photomultiplier tube (Model H10720-20) from Hamamatsu, using time-correlated single-photon counting. All time-resolved measurements were performed at the same excitation power density (P). PL lifetimes were calculated from the measured decay kinetics with the FAST software (Edinburgh Instruments) using a second-order exponential decay fit. The decay curves of the long-lived UCL were used as obtained, without consideration of the instrument response function (tail fit, no unfolding of the instrument response function was done).

Hard X-Ray Photoemission Spectroscopy: The hard X-ray photoemission spectroscopy (HAXPES) measurements were performed at the KMC-1 beamline (photon energy range, 2003–12 000 eV) at the BESSY II synchrotron[77] using the SpAnTeX endstation. The SpAnTeX endstation is equipped with a PHOIBOS 150 HV NAP analyzer and is capable of measuring up to 10 keV kinetic energy electrons. Details of the SpAnTeX endstation can be found elsewhere.[78] The UCNPs were drop casted onto a clean piece of copper foil and the solvent was evaporated with heating at 60 °C. The samples were measured in grazing incidence and normal emission. The area of the sample measured was determined by the circular entrance aperture of the electron spectrometer, which is 300 µm in diameter, and therefore many particles with a variety of orientations were averaged over. The photon flux was monitored with an ionization chamber filled with N_2(g) and kept constant throughout the measurements at a set photon energy. Sets of core levels at each photon energy were collected cyclically (i.e., cycling of sequential single scans for each core level) helping to minimize any influence of X-ray flux changes on the peak intensity ratios. By only comparing peak intensity ratios at the same photon energy, and collecting the data in the cyclic mode, the need for any correction to the peak intensities for relative

changes in the photon flux was eliminated. Lastly, a pass energy of 30 eV and a step size of 0.05 eV was used to collect the spectra.

Shirley background functions were subtracted from all spectra. The areas of the Er $3d_{5/2}$ and Yb $3d_{5/2}$ peaks were integrated (including the satellite peaks) after subtracting the Shirley background, while other core levels (F 1s, Na 1s, Na 2s, C 1s) were fitted using symmetric pseudo-Voigt functions (G/L ratios between 15/85 to 30/70) to extract the integrated peak areas. Photoionization cross-sections were calculated using tabulated values including non-dipole effects, in the regime for linearly polarized light (see Supporting Information), and used to translate peak intensity ratios to concentration ratios.[79,80] Inelastic mean free paths were calculated with the TPP-2M formula for $NaYF_4$.[81] Concentration ratios were plotted as a function of kinetic energy where the average kinetic energy of the Er $3d_{5/2}$ and Yb $3d_{5/2}$ levels was used. Standard deviations of the concentration ratios were calculated from the variation in the integrated peak areas when changing the background region used to fit the Er^{3+} and Yb^{3+} peaks. Note that no error associated with the calculated cross-sections was included.

Potential beam damage over the duration of the experiment was examined by repeating the measurement of Er $3d_{5/2}$ and Yb $3d_{5/2}$ core levels of sample C (with 2970 eV photon energy in the same position on the sample) measured 18 h apart. During these 18 h the rest of the depth-profiling measurements were conducted. The ratio of $[Er^{3+}]/[Yb^{3+}]$ was consistent between the before and after measurements and no structural change was found between the spectra (Figure S15, Supporting Information), leading to the conclusion that no beam damage occurred to the nanoparticles nor affected the dopant ratios.

SESSA Simulation Details: The program SESSA (SESSA, v2.1) was used to simulate the HAXPES results for the three types of nanoparticles.[53] Full details of the parameters used for the SESSA simulations can be found in the Supporting Information. These simulations assume that the particles were spheres with uniform shells, when shells were included in the model. The diameter of spheres used in the simulations for particles A, B, and C were calculated so that the sphere volume was equal to the average volume of the UCNPs as determined from the TEM size distributions. Tests of different-sized spheres showed that the overall size made negligible difference to the simulation results for diameters >20 nm. Specific chemical stoichiometries for the UCNPs were used to simulate the data with SESSA. However, since peak area ratios obtained from the SESSA simulations were compared to those measured with HAXPES depth-profiling, using other chemical stoichiometries for the SESSA simulations that have the same dopant ion concentration ratios will lead to the same peak area ratio from SESSA, and will compare equally as well to the peak area ratio from the HAXPES depth-profiling. All models were made with stoichiometries of NaY_xF_4:Er^{3+}_y, Yb^{3+}_z where $x = 1 - y - z$. The peak area ratios from the SESSA simulations were then cross-section corrected to convert to elemental ratios, $[Er^{3+}]/[Yb^{3+}]$. A satisfactory match to the experimental data was defined as being within one standard deviation at each kinetic energy (see above).

Inductively Coupled Plasma—Optical Emission Spectroscopy Measurements: Quantification of the lanthanide ions was done using inductively coupled plasma—optical emission spectroscopy (ICP-OES) with a SPECTRO Arcos-EOP (Model: FHX, 76004553) spectrometer. The ICP standard solutions (1000 mg L^{-1} in nitric acid (2–3%)) used for the calibration required for the quantification were purchased from Sigma Aldrich. The calibration was performed with 10 standard solutions covering the range of 0–2000 µg L^{-1}, 0–200 µg L^{-1}, and 0–7200 µg L^{-1} for Yb^{3+}, Er^{3+}, and Y^{3+}, respectively. The samples were dried, dissolved in nitric acid, and further diluted in milliQ water prior to the measurements.

Supporting Information

Supporting Information is available from the Wiley Online Library or from the author.

Acknowledgements

The SpAnTeX end-station was supported by the Helmholtz Association through the Helmholtz Energy Materials Foundry (HEMF, GZ 714-48172-21/1), and is operated within the Berlin joint laboratory for ElectroChemical interfaces (BElChem). The authors thank Marcel Mertin for his technical assistance at the KMC1 beamline, Ulrike Blöck for her assistance with the TEM measurements, André Gardei (BAM) for assistance with the XRD measurements, Janina Roik (BAM, Division 1.6) for assistance with the ICP-OES measurements, and Abdelkrim Chemseddine for his advice on nanoparticle synthesis for sample C. EA gratefully acknowledges support from the German Research Council (DFG, grant SCHA 1009/17-1)) and the Federal Ministry of Economic Affairs and Climate Action (BMWK, funding program ZIM, project FluoMat (grant ZF4044237ZG9)) and URG acknowledges support from the BAM-financed internal project *nanoplatform*.

Open access funding enabled and organized by Projekt DEAL.

Conflict of Interest

The authors declare no conflict of interest.

Data Availability Statement

The data that support the findings of this study are available from the corresponding author upon reasonable request.

Keywords

core@shell, depth profile, dopant distributions, interfaces, nanoparticles, photoelectron spectroscopy, upconversion

Received: December 23, 2021
Revised: May 25, 2022
Published online: June 22, 2022

[1] Q. Zhang, F. Yang, Z. Xu, M. Chaker, D. Ma, *Nanoscale Horiz.* **2019**, *4*, 579.
[2] H. Dong, S.-R. Du, X.-Y. Zheng, G.-M. Lyu, L.-D. Sun, L.-D. Li, P.-Z. Zhang, C. Zhang, C.-H. Yan, *Chem. Rev.* **2015**, *115*, 10725.
[3] Z. Xue, X. Li, Y. Li, M. Jiang, G. Ren, H. Liu, S. Zeng, J. Hao, *Nanoscale* **2017**, *9*, 7276.
[4] M. Wang, T. Zhang, Y. Hu, Y. Qin, W. Wei, *ChemPhotoChem* **2019**, *3*, 145.
[5] L. Xiong, Z. Chen, Q. Tian, T. Cao, C. Xu, F. Li, *Anal. Chem.* **2009**, *81*, 8687.
[6] E. Hemmer, P. Acosta-Mora, J. Méndez-Ramos, S. Fischer, *J. Mater. Chem. B* **2017**, *5*, 4365.
[7] M. Tan, F. Li, N. Cao, H. Li, X. Wang, C. Zhang, D. Jaque, G. Chen, *Small* **2020**, *16*, 2004118.
[8] D. Jaque, F. Vetrone, *Nanoscale* **2012**, *4*, 4301.
[9] C. Wang, L. Cheng, Z. Liu, *Biomaterials* **2011**, *32*, 1110.
[10] A. Bagheri, H. Arandiyan, C. Boyer, M. Lim, *Adv. Sci.* **2016**, *3*, 1500437.
[11] Y. Liu, Y. Feng, C. Xu, H. He, Y. Zhang, Z. Xu, L. Li, J. Wang, *Part. Part. Syst. Charact.* **2019**, *36*, 1900200.
[12] Y. Shang, S. Hao, C. Yang, G. Chen, *Nanomaterials* **2015**, *5*, 1782.
[13] S. Hao, Y. Shang, D. Li, H. Ågren, C. Yang, G. Chen, *Nanoscale* **2017**, *9*, 6711.
[14] X. Liu, L. T. Su, S. K. Karuturi, J. Luo, L. Liu, X. Liu, J. Guo, T. C. Sum, R. Deng, H. J. Fan, A. I. Y. Tok, *Adv. Mater.* **2013**, *25*, 1603.

[15] K. Feng, Z. Cai, H. Dingwang, L. Li, K. Wang, Y. Li, C. Wang, J. Song, L. Zhao, W. Wei, F. Jiang, *Sustainable Energy Fuels* **2020**, *4*, 2669.
[16] X. Chen, L. Jin, W. Kong, T. Sun, W. Zhang, X. Liu, J. Fan, S. F. Yu, F. Wang, *Nat. Commun.* **2016**, *7*, 10304.
[17] J. Zhou, Q. Liu, W. Feng, Y. Sun, F. Li, *Chem. Rev.* **2015**, *115*, 395.
[18] A. Fernandez-Bravo, D. Wang, E. S. Barnard, A. Teitelboim, C. Tajon, J. Guan, G. C. Schatz, B. E. Cohen, E. M. Chan, P. J. Schuck, T. W. Odom, *Nat. Mater.* **2019**, *18*, 1172.
[19] J. Wang, R. Deng, M. A. Macdonald, B. Chen, J. Yuan, F. Wang, D. Chi, T. S. Andy Hor, P. Zhang, G. Liu, Y. Han, X. Liu, *Nat. Mater.* **2014**, *13*, 157.
[20] B. Chen, F. Wang, *Acc. Chem. Res.* **2019**, *53*, 358.
[21] H. Dong, L. D. Sun, C. H. Yan, *Chem. Soc. Rev.* **2015**, *44*, 1608.
[22] A. Nadort, J. Zhao, E. M. Goldys, *Nanoscale* **2016**, *8*, 13099.
[23] C. Würth, M. Kaiser, S. Wilhelm, B. Grauel, T. Hirsch, U. Resch-Genger, *Nanoscale* **2017**, *9*, 4283.
[24] Y. Hu, Q. Shao, Y. Dong, J. Jiang, *J. Phys. Chem. C* **2019**, *123*, 22674.
[25] C. Homann, L. Krukewitt, F. Frenzel, B. Grauel, C. Würth, U. Resch-Genger, M. Haase, *Angew. Chem., Int. Ed.* **2018**, *57*, 8765.
[26] J. Zuo, Q. Li, B. Xue, C. Li, Y. Chang, Y. Zhang, X. Liu, L. Tu, H. Zhang, X. Kong, *Nanoscale* **2017**, *9*, 7941.
[27] F. Wang, J. Wang, X. Liu, *Angew. Chem., Int. Ed.* **2010**, *49*, 7456.
[28] F. Zhang, R. Che, X. Li, C. Yao, J. Yang, D. Shen, P. Hu, W. Li, D. Zhao, *Nano Lett.* **2012**, *12*, 2852.
[29] X. Li, D. Shen, J. Yang, C. Yao, R. Che, F. Zhang, D. Zhao, *Chem. Mater.* **2013**, *25*, 106.
[30] S. Fischer, N. D. Bronstein, J. K. Swabeck, E. M. Chan, A. P. Alivisatos, *Nano Lett.* **2016**, *16*, 7241.
[31] C. Würth, S. Fischer, B. Grauel, A. P. Alivisatos, U. Resch-Genger, *J. Am. Chem. Soc.* **2018**, *140*, 4922.
[32] D. Hudry, I. A. Howard, R. Popescu, D. Gerthsen, B. S. Richards, *Adv. Mater.* **2019**, *31*, 1900623.
[33] Z. Wang, A. Meijerink, *J. Phys. Chem. C* **2018**, *122*, 26298.
[34] N. J. J. Johnson, S. He, S. Diao, E. M. Chan, H. Dai, A. Almutairi, *J. Am. Chem. Soc.* **2017**, *139*, 3275.
[35] B. Shen, S. M. Cheng, Y. Y. Gu, D. R. Ni, Y. L. Gao, Q. Q. Su, W. Feng, F. Y. Li, *Nanoscale* **2017**, *9*, 1964.
[36] X. Liu, X. Kong, Y. Zhang, L. Tu, Y. Wang, Q. Zeng, C. Li, Z. Shi, H. Zhang, *Chem. Commun.* **2011**, *47*, 11957.
[37] F. Wang, R. Deng, J. Wang, Q. Wang, Y. Han, H. Zhu, X. Chen, X. Liu, *Nat. Mater.* **2011**, *10*, 968.
[38] C. Ma, X. Xu, F. Wang, Z. Zhou, D. Liu, J. Zhao, M. Guan, C. I. Lang, D. Jin, *Nano Lett.* **2017**, *17*, 2858.
[39] Y. Shang, S. Hao, W. Lv, T. Chen, L. Tian, Z. Lei, C. Yang, *J. Mater. Chem. C* **2018**, *6*, 3869.
[40] F. Vetrone, R. Naccache, V. Mahalingam, C. G. Morgan, J. A. Capobianco, *Adv. Funct. Mater.* **2009**, *19*, 2924.
[41] X. Huang, J. Lin, *J. Mater. Chem. C* **2015**, *3*, 7652.
[42] S. Wen, J. Zhou, K. Zheng, A. Bednarkiewicz, X. Liu, D. Jin, *Nat. Commun.* **2018**, *9*, 2415.
[43] B. Chen, F. Wang, *Acc. Chem. Res.* **2020**, *53*, 358.
[44] W. Wei, Y. Zhang, R. Chen, J. Goggi, N. Ren, L. Huang, K. K. Bhakoo, H. Sun, T. T. Y. Tan, *Chem. Mater.* **2014**, *26*, 5183.
[45] D. Hudry, A. De Backer, R. Popescu, D. Busko, I. A. Howard, S. Bals, Y. Zhang, A. Pedrazo-Tardajos, S. Van Aert, D. Gerthsen, T. Altantzis, B. S. Richards, *Small* **2021**, *17*, 2104441.
[46] P. C. J. Clark, N. K. Lewis, J. C.-R. Ke, R. Ahumada-Lazo, Q. Chen, D. C. J. Neo, E. A. Gaulding, G. F. Pach, I. Pis, M. G. Silly, W. R. Flavell, *Nanoscale* **2021**, *13*, 17793.
[47] P. C. J. Clark, D. C. J. Neo, R. Ahumada-Lazo, A. I. Williamson, I. Pis, S. Nappini, A. A. R. Watt, W. R. Flavell, *Langmuir* **2018**, *34*, 8887.
[48] P. C. J. Clark, H. Radtke, A. Pengpad, A. I. Williamson, B. F. Spencer, J. O. Hardman, M. A. Leontiadou, D. C. J. Neo, S. M. Fairclough, A. A. R. Watt, I. Pis, S. Nappini, F. Bondino, E. Magnano, K. Schulte, M. Silly, F. Sirotti, W. R. Flavell, *Nanoscale* **2017**, *9*, 6056.
[49] K. A. Abel, J. C. Boyer, F. C. J. M. Van Veggel, *J. Am. Chem. Soc.* **2009**, *131*, 14644.
[50] J. Pichaandi, G. K. Das, N. J. J. Johnson, T. Regier, F. C. J. M. Van Veggel, *J. Phys. Chem. C* **2014**, *118*, 21639.
[51] X. Xu, C. Clarke, C. Ma, G. Casillas, M. Das, M. Guan, D. Liu, L. Wang, A. Tadich, Y. Du, C. Ton-That, D. Jin, *Nanoscale* **2017**, *9*, 7719.
[52] J. Radnik, X. Knigge, E. Andresen, U. Resch-Genger, D. J. H. Cant, A. G. Shard, C. A. Clifford, *Anal. Bioanal. Chem.* **2022**, *414*, 4331.
[53] W. S. M. Werner, W. Smekal, C. J. Powell, *Simulation of Electron Spectra for Surface Analysis (SESSA) – Version 2.1*, National Institute Of Standards And Technology, Gaithersburg, MD, **2016**.
[54] S. Wilhelm, M. Kaiser, C. Würth, J. Heiland, C. Carrillo-Carrion, V. Muhr, O. S. Wolfbeis, W. J. Parak, U. Resch-Genger, T. Hirsch, *Nanoscale* **2015**, *7*, 1403.
[55] J. C. Boyer, F. Vetrone, L. A. Cuccia, J. A. Capobianco, *J. Am. Chem. Soc.* **2006**, *128*, 7444.
[56] T. Cong, Y. Ding, S. Xin, X. Hong, H. Zhang, Y. Liu, *Langmuir* **2016**, *32*, 13200.
[57] I. Hyppänen, N. Höysniemi, R. Arppe, M. Schäferling, T. Soukka, *J. Phys. Chem. C* **2017**, *121*, 6924.
[58] S. Wu, Y. Ning, J. Chang, S. Zhang, *J. Lumin.* **2013**, *143*, 492.
[59] M. Kraft, C. Würth, V. Muhr, T. Hirsch, U. Resch-Genger, *Nano Res.* **2018**, *11*, 6360.
[60] D. T. Klier, M. U. Kumke, *J. Mater. Chem. C* **2015**, *3*, 11228.
[61] D. Saleta Reig, B. Grauel, V. A. Konyushkin, A. N. Nakladov, P. P. Fedorov, D. Busko, I. A. Howard, B. S. Richards, U. Resch-Genger, S. V. Kuznetsov, A. Turshatov, C. Würth, *J. Mater. Chem. C* **2020**, *8*, 4093.
[62] J. Liu, T. Fu, C. Shi, *J. Phys. Chem. C* **2019**, *123*, 9506.
[63] A. A. Abozeed, T. Kadono, A. Sekiyama, H. Fujiwara, A. Higashiya, A. Yamasaki, Y. Kanai, K. Yamagami, K. Tamasaku, M. Yabashi, T. Ishikawa, A. V. Andreev, H. Wada, S. Imada, *J. Phys. Soc. Jpn.* **2018**, *87*, 033710.
[64] H. Sato, Y. Utsumi, K. Katoh, K. Mimura, S. Ueda, H. Yamaoka, A. Rousuli, M. Arita, K. Umeo, K. Shimada, H. Namatame, M. Taniguchi, *Phys. Status Solidi C* **2017**, *14*, 1600164.
[65] L. Moreschini, C. Dallera, J. J. Joyce, J. L. Sarrao, E. D. Bauer, V. Fritsch, S. Bobev, E. Carpene, S. Huotari, G. Vankó, G. Monaco, P. Lacovig, G. Panaccione, A. Fondacaro, G. Paolicelli, P. Torelli, M. Grioni, *Phys. Rev. B: Condens. Matter Mater. Phys.* **2007**, *75*, 035113.
[66] J. Yamaguchi, A. Sekiyama, S. Imada, H. Fujiwara, M. Yano, T. Miyamachi, G. Funabashi, M. Obara, A. Higashiya, K. Tamasaku, M. Yabashi, T. Ishikawa, F. Iga, T. Takabatake, S. Suga, *Phys. Rev. B: Condens. Matter Mater. Phys.* **2009**, *79*, 125121.
[67] K. Kuga, Y. Kanai, H. Fujiwara, K. Yamagami, S. Hamamoto, Y. Aoyama, A. Sekiyama, A. Higashiya, T. Kadono, S. Imada, A. Yamasaki, K. Tamasaku, M. Yabashi, T. Ishikawa, S. Nakatsuji, T. Kiss, *J. Electron Spectrosc. Relat. Phenom.* **2020**, *238*, 146889.
[68] W. H. Doh, V. Papaefthimiou, T. Dintzer, V. Dupuis, S. Zafeiratos, *J. Phys. Chem. C* **2014**, *118*, 26621.
[69] M. Fondell, M. Gorgoi, M. Boman, A. Lindblad, *J. Electron Spectrosc. Relat. Phenom.* **2018**, *224*, 23.
[70] S. Tanuma, C. J. Powell, D. R. Penn, *Surf. Interface Anal.* **1994**, *21*, 165.
[71] S. Hüfner, *Photoelectron Spectroscopy Principles and Applications*, Springer, Berlin **2003**.
[72] Q. Liu, Y. Zhang, C. S. Peng, T. Yang, L. M. Joubert, S. Chu, *Nat. Photonics* **2018**, *12*, 548.
[73] J. Zhou, S. Xu, J. Zhang, J. Qiu, *Nanoscale* **2015**, *7*, 15026.
[74] S. Wu, G. Han, D. J. Milliron, S. Aloni, V. Altoe, D. V. Talapin, B. E. Cohen, P. J. Schuck, *Proc. Natl. Acad. Sci. USA* **2009**, *106*, 10917.

[75] F. Frenzel, C. Würth, O. Dukhno, F. Przybilla, L. M. Wiesholler, V. Muhr, T. Hirsch, Y. Mély, U. Resch-Genger, *Nano Res.* **2021**, *14*, 4107.
[76] N. Bogdan, F. Vetrone, G. A. Ozin, J. A. Capobianco, *Nano Lett.* **2011**, *11*, 835.
[77] F. Schaefers, M. Mertin, M. Gorgoi, *Rev. Sci. Instrum.* **2007**, *78*, 123102.
[78] M. Favaro, P. C. J. Clark, M. J. Sear, M. Johansson, S. Maehl, R. Van De Krol, D. E. Starr, *Surf. Sci.* **2021**, *713*, 121903.
[79] M. B. Trzhaskovskaya, V. I. Nefedov, V. G. Yarzhemsky, *At. Data Nucl. Data Tables* **2002**, *82*, 257.
[80] M. B. Trzhaskovskaya, V. K. Nikulin, V. I. Nefedov, V. G. Yarzhemsky, *At. Data Nucl. Data Tables* **2006**, *92*, 245.
[81] S. Tanuma, C. J. Powell, D. R. Penn, *Surf. Interface Anal.* **2003**, *35*, 268.